

Comparison of beam emission spectroscopy and gas puff imaging edge fluctuation measurements in National Spherical Torus Experiment

Y. Sechrest, D. Smith, D. P. Stotler, T. Munsat, and S. J. Zweben

Citation: *Physics of Plasmas* **22**, 052310 (2015); doi: 10.1063/1.4921215

View online: <http://dx.doi.org/10.1063/1.4921215>

View Table of Contents: <http://scitation.aip.org/content/aip/journal/pop/22/5?ver=pdfcov>

Published by the [AIP Publishing](#)

Articles you may be interested in

[Edge electron density profiles and fluctuations measured by two-dimensional beam emission spectroscopy in the KSTARa\)](#)

Rev. Sci. Instrum. **85**, 11E434 (2014); 10.1063/1.4894839

[Comparison of scrape-off layer turbulence simulations with experiments using a synthetic gas puff imaging diagnostic](#)

Phys. Plasmas **18**, 022306 (2011); 10.1063/1.3553024

[Flow and shear behavior in the edge and scrape-off layer of L-mode plasmas in National Spherical Torus Experiment](#)

Phys. Plasmas **18**, 012502 (2011); 10.1063/1.3533435

[Development of KSTAR ECE imaging system for measurement of temperature fluctuations and edge density fluctuationsa\)](#)

Rev. Sci. Instrum. **81**, 10D930 (2010); 10.1063/1.3483209

[Study of statistical properties of edge turbulence in the National Spherical Torus Experiment with the gas puff imaging diagnostic](#)

Phys. Plasmas **14**, 102305 (2007); 10.1063/1.2776912



www.trekinc.com



HIGH-VOLTAGE AMPLIFIERS AND ELECTROSTATIC VOLTMETERS

ENABLING RESEARCH AND INNOVATION IN DIELECTRICS, MICROFLUIDICS, MATERIALS, PLASMAS AND PIEZOS

Comparison of beam emission spectroscopy and gas puff imaging edge fluctuation measurements in National Spherical Torus Experiment

Y. Sechrest,¹ D. Smith,² D. P. Stotler,³ T. Munsat,¹ and S. J. Zweben³

¹Department of Physics, University of Colorado, Boulder, Colorado 80309, USA

²Department of Engineering Physics, University of Wisconsin-Madison, Madison, Wisconsin 53706, USA

³Princeton Plasma Physics Laboratory, Princeton, New Jersey 08540, USA

(Received 1 April 2015; accepted 5 May 2015; published online 26 May 2015)

In this study, the close physical proximity of the Gas Puff Imaging (GPI) and Beam Emission Spectroscopy (BES) diagnostics on the National Spherical torus Experiment (NSTX) is leveraged to directly compare fluctuation measurements, and to study the local effects of the GPI neutral deuterium puff during H-mode plasmas without large Edge Localized Modes. The GPI and BES views on NSTX provide partially overlapping coverage of the edge and scrape-off layer (SOL) regions above the outboard midplane. The separation in the toroidal direction is 16° , and field lines passing through diagnostic views are separated by ~ 20 cm in the direction perpendicular to the magnetic field. Strong cross-correlation is observed, and strong cross-coherence is seen for frequencies between 5 and 15 kHz. Also, probability distribution functions of fluctuations measured ~ 3 cm inside the separatrix exhibit only minor deviations from a normal distribution for both diagnostics, and good agreement between correlation length estimates, decorrelation times, and structure velocities is found at the $\pm 40\%$ level. While the two instruments agree closely in many respects, some discrepancies are observed. Most notably, GPI normalized fluctuation levels exceed BES fluctuations by a factor of ~ 9 . BES mean intensity is found to be sensitive to the GPI neutral gas puff, and BES normalized fluctuation levels for frequencies between 1 and 10 kHz are observed to increase during the GPI puff. © 2015 AIP Publishing LLC. [<http://dx.doi.org/10.1063/1.4921215>]

I. INTRODUCTION

Understanding the physics of the edge and pedestal regions of tokamak plasmas is essential to the operation of high performance fusion devices. Turbulence in the edge enhances transport above neoclassical levels which severely limits the achievable confinement. Experiments have observed that during the transition to high confinement (H-mode) an edge transport barrier (ETB) is formed, and a suppression of the transport is achieved.^{1–3} The reduced transport at the edge leads to a buildup of pressure with steep gradients in temperature and density. This yields a “pedestal” in the density and temperature profiles that the core profiles sit atop, thus the height and width of the pedestal significantly impact the achievable performance of the device. The steep gradients of the pedestal provide a source of free-energy for MHD instabilities localized to the edge, accordingly called Edge Localized Modes (ELMs), which can exhaust large amounts of stored energy and particles. These ELMs can damage plasma facing components; therefore, controlling ELMs is a major concern for current and next-step fusion devices.⁴ The nature of microturbulence that drives transport in the edge, the development of the ETB during the L-H transition and subsequent suppression of turbulence, the evolution of the pedestal, and the dynamics of ELMs all underscore the importance of understanding this region of the plasma, and the need for highly resolved diagnostic information.

Two diagnostics that have been used extensively to study the pedestal and edge regions are Beam Emission Spectroscopy (BES) and Gas Puff Imaging (GPI). BES has

been used to measure density fluctuations on many major Tokamak experiments of the past 2 decades. As the name suggests, BES measures fluctuations in the plasma density via spectroscopy of radiation from the interaction of an energetic beam of neutral particles, either a neutral beam injection (NBI) heating beam or a separate diagnostic beam, with the plasma. The diagnostic has been used to study a number of phenomena relevant to the plasma edge, including characterization of low-wavenumber ($k_\perp \rho_s \lesssim 1$) turbulence,^{5,6} measurement of turbulent and zonal flows,^{7–9} and turbulence-generated coherent structures.¹⁰

GPI has also been used on a number of fusion experiments including NSTX, Alcator C-mod, TEXTOR, RFX-mod, and EAST.^{11–15} Similar to BES, GPI measures visible light fluctuations from the interaction of neutrals with the plasma, but the neutral source is a puff of thermal gas, usually helium or deuterium, from a gas nozzle located on the vessel wall. GPI has been used to study edge turbulence and blobs,^{11,12,16–19} turbulent velocity fields,^{20–24} ELMs,^{25,26} and L-H transitions.^{22,27}

In addition to the experimental work, significant work has been done to model the atomic physics processes relevant to both diagnostics. Collisional radiative models have been developed to better understand the penetration of neutral beams into plasma, and to provide the physical basis for BES and other active spectroscopy diagnostics.^{28–34} Collisional radiative models have also been used to explain GPI emission profiles, and simulations have been performed to examine the transport of the neutral gas puff in the edge.^{35–38} Both diagnostics are concerned with measuring the Balmer- α line emission which has the form $I = A_{32}n_0f_3$,

where A_{32} is the Einstein coefficient for spontaneous emission, n_0 is population of the neutral ground state, and f_3 is the ratio of density of the excited level to the ground state. The collisional radiative models are concerned with accurately predicting the population of states, and thus this ratio, f_3 . For BES, f_3 is usually simplified to be a function of only plasma density, but GPI typically requires the retention of both the electron density and temperature. For densities and temperatures corresponding to typical H-mode pedestals on NSTX, however, GPI emission can, to a good approximation, also be considered to be a function of only the electron density. Therefore, GPI and BES are expected to measure predominantly density fluctuations.

In this study, we carry out the direct comparison of measurements of edge turbulence made with the BES and GPI diagnostics in H-mode operation that is free of large ELMs. This study tests our understanding of the operation of, and interpretation of data from these two diagnostics. The goal of this comparison is to provide experimental verification that the measurements agree where modeling of diagnostic response suggests they should, and that observations are consistent between the two diagnostics. In addition to increased confidence in the measurements that this provides, this study lays the groundwork to use the diagnostics more collaboratively in the future. Furthermore, the relatively close proximity of the BES viewing volume to the GPI gas manifold allows the local effects of the GPI neutral gas puff on the BES measurements to be quantified.

The remainder of the paper is organized as follows: Sec. II discusses the GPI and BES diagnostics, the relative positioning of the two, and NSTX operation. Section III compares measurements of relative fluctuation levels and fluctuation probability density functions. Section IV describes cross-diagnostic correlation and coherence analysis. Section V compares statistical analysis of fluctuations between the two diagnostics. Section VI discusses the estimation of poloidal correlation lengths and decorrelation times, and estimates of these quantities are compared. Section VII provides discussion of the results, and Sec. VIII summarizes the results.

II. EXPERIMENTAL DETAILS

A. Gas puff imaging diagnostic

Gas Puff Imaging is a diagnostic technique used to image visible light fluctuations from collisional excitation of neutral atoms by plasma electrons. The details of the diagnostic have been discussed at length in previous work,^{11,12,39,40} so only a brief review is included here. The NSTX GPI system consists of a gas manifold and a fast-framing camera. The manifold is a 29 cm long pipe perforated by thirty 1 mm diameter holes spaced evenly along its length. The gas manifold is located just inside the vacuum vessel wall 20 cm above the outboard midplane, and it discharges a neutral D_2 gas puff. The neutral gas penetrates into the edge of the plasma, dissociates, becomes excited by collisions with plasma electrons, and radiatively decays. The visible light emission (D_2 ; $n = 3 \rightarrow 2$; 656 nm) from this process is transferred from a collecting lens through a

fiber-optic bundle, passed through an interference filter, and imaged by a Phantom v710 fast-framing camera. Images of 64×80 pixels are taken at 400 kHz frame rate ($2.5 \mu\text{s}$ per frame) with an exposure time of $2.2 \mu\text{s}$. Numerical modeling of the atomic physics processes has shown that the light emission may be approximated by the function $I_{GPI} = n_0 F(n_e, T_e)$, where F represents the photon emission rate per atom.^{37,40} Inserting the approximate functional form for the n_e and T_e dependence yields $I_{GPI} \propto n_0 n_e^\alpha T_e^\beta$, where the exponents α and β vary with the plasma parameters across the GPI view.

The optical view is tilted by $\sim 40^\circ$ with respect to horizontal so that the view is approximately aligned with the local direction of the magnetic field at the intersection with the gas puff during standard operation. The x and y coordinates of the camera image are approximately perpendicular and tangent to surfaces of constant flux, respectively. Thus, the image x coordinate is approximately the radial coordinate, and the y coordinate is then the generalized poloidal coordinate. Note that this is not the machine poloidal direction which lies in the R-Z plane, but instead the generalized poloidal direction lies in the plane perpendicular to the local magnetic field. For the shots studied here, the axes of the GPI view differ from the generalized poloidal and radial directions by $\leq 10^\circ$. In this study, we refer to the generalized poloidal direction simply as the poloidal direction.

The pixel resolution at the location of the gas puff is $3.8 \text{ mm} \times 3.8 \text{ mm}$, and the total viewable area is $24 \text{ cm} \times 30 \text{ cm}$. The positioning of the GPI and BES diagnostics is discussed in Sec. IID, and an illustration of the GPI view is shown in Fig. 1(a). The toroidal extent of the gas cloud coupled with the curvature of the magnetic field line acts to degrade the radial resolution. Similarly, the poloidal

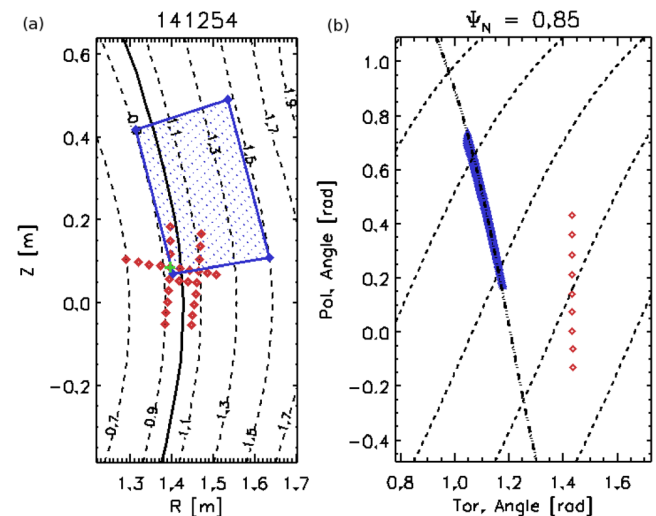


FIG. 1. (a) $R = 140$ cm BES channel positions (red diamonds) and GPI viewing area (blue polygon) plotted over contours of poloidal flux for NSTX shot 141254. Flux surfaces are labeled by their midplane r/a value, and the separatrix is indicated by the solid black line. BES channel positions and the corners of the GPI view are plotted using cylindrical coordinates. Green cross indicates BES channel used for comparison. (b) BES inner poloidal array (red diamonds) plotted in toroidal coordinates with GPI points (blue) for similar flux value. Magnetic field line traces are plotted as dashed lines, and the dotted-dashed line traces the generalized poloidal direction.

resolution is degraded by any misalignment of the camera viewing angle with the magnetic field line pitch angle. Experimental observations of the width of the gas cloud combined with field line curvature yield an effective radial resolution of $\Delta_r \approx 2 \pm 1$ cm, and the poloidal resolution is between $0.5 \leq \Delta_{pol} \leq 2.0$ cm depending on the degree of misalignment.³⁹ For this study, the misalignment is $\leq 10^\circ$, so the poloidal resolution is close to 0.5 cm for all shots. For typical NSTX edge parameters, the GPI light emission is localized to the region with $T_e, T_i \lesssim 0.3$ keV and ion sound gyroradius $\rho_s \lesssim 1$ cm. Thus, fluctuations that satisfy $\langle k_{pol} \rangle \rho_s = \pi \rho_s / \Delta_{POL} \lesssim 6.0$, including typical drift turbulence scales⁴¹ of $\langle k_{pol} \rangle \rho_s \approx 0.1 - 1$, are well resolved by the GPI diagnostic.

B. Beam emission spectroscopy diagnostic

Similar to the GPI diagnostic, the Beam Emission Spectroscopy diagnostic measures light emission from the collisional excitation of neutral atoms. Where the GPI diagnostic uses a gas puff to localize the observation, the BES diagnostic images D_α line emission that is localized to the intersection of optical sight lines with the neutral heating beam. The velocity of beam neutrals in combination with the viewing geometry produces a Doppler shift, which isolates the beam D_α line from thermal emission from the bulk plasma. The D_α emission is collected by a high-throughput optical assembly and imaged onto a set of optical fiber bundles. The fiber bundles transmit the light to a set of collimating lenses and transmission filters that selectively pass the Doppler shifted D_α emission. Finally, PIN photodiodes measure the D_α light intensity. The dependence of measured emission on plasma parameters has been studied (see Ref. 31 and references therein for review), and for typical parameters in the NSTX pedestal the light emission can be approximated by $\delta I_{BES} / \langle I_{BES} \rangle \approx 0.5 \delta n_e / \langle n_e \rangle$ for modest fluctuation levels, $\delta n_e / \langle n_e \rangle \leq 10\%$.^{31,42} The sensitivity of light emission to other parameters, including temperature, is found to be much weaker than the density dependence.

The NSTX BES system, discussed in detail in Refs. 43 and 44, consists of two separate optical assemblies with one view centered at $R = 130$ cm ($r/a \approx 0.7$) and another view at $R = 140$ cm ($r/a \approx 0.9$). For this study, we make use of only the outer 28 channel assembly, and an illustration of the channel positions is presented in Fig. 1. The radial array provides coverage from $r/a \approx 0.7$ to well into the scrape-off layer, and two poloidal arrays are positioned at $r/a \approx 0.9$ and in the scrape-off layer. The optical view is aligned with the local magnetic field at the position of the heating beam, an angle of 37° with respect to horizontal, to optimize cross-field resolution. Spot-sizes at the neutral beam cross-section are 2–3 cm, and detailed point-spread function calculations indicate minor image distortions from field line misalignment and atomic state lifetimes. Thus, turbulent fluctuations with $k_\perp \rho_s \leq 1.5$ are well resolved. Data are acquired at a 2 MHz sampling rate, and frequency-compensating, wide-band preamplifiers provide photon-noise limited measurements at frequencies up to 400 kHz.

C. NSTX operation

The shots selected for this study are from a subset of the NSTX 2010 run campaign in which both the GPI and BES diagnostics were operational, and each shot is chosen to be free of large ELM events during the GPI observing period. Table I details the list of chosen shots and shot parameters. The shots are selected from 2 different experiments carried out on different run days. Typical n_e and T_e profiles for these shots are plotted in Fig. 2 along with the GPI emission profiles. The red dashed line indicates the radial location of the $R = 140$ cm BES radial channel used for the comparison. The GPI light emission is localized around the last closed flux surface (LCFS), and the light emission decays to its half maximum value near the normalized flux value, Ψ_N of 0.8. This position corresponds to densities of $2 - 5 \times 10^{13}$ cm⁻³ and temperatures of 100 – 200 eV. The $R = 140$ cm BES assembly has radial views located at normalized flux values between ~ 0.3 and 1.2, spanning the scrape-off layer (SOL), gradient region, and pedestal top. This study focuses on the near-SOL and gradient region to compare with the GPI measurements.

D. Relative diagnostic positioning

A schematic representation of the BES and GPI views is illustrated in Figs. 1(a) and 1(b). Fig. 1(a) shows the relative position of the GPI view (blue polygon) and the BES channels (red diamonds) in the (R, Z) plane. BES channels and corners of the GPI view are plotted using their cylindrical R and Z coordinates, ignoring the different toroidal angles. Flux surfaces are indicated by dashed contours and labeled with their midplane r/a value, and the separatrix is indicated by the solid black contour. In Fig. 1(b), The BES inner poloidal array channels (red diamonds) are plotted in toroidal and machine-poloidal coordinates along with GPI pixels (blue points) with similar values of poloidal flux. Magnetic field line traces in these coordinates are indicated by dashed lines, and a trace of the generalized poloidal coordinate passing through the GPI points is indicated by the dotted-dashed line.

The GPI view is centered 28° above the outboard midplane, and the radial extent of the view typically captures the edge region, separatrix, and SOL. The $R = 140$ cm BES assembly is positioned at 12° above the outboard midplane and provides similar radial coverage. The separation between the lower-left corner of the GPI view and the intersection of the BES radial and inner poloidal array, as seen in Fig. 1(b), is 16° in the toroidal direction and 3° in the poloidal direction.

TABLE I. Shot list for this study containing the shot number, toroidal field at the magnetic axis, plasma current, neutral beam heating power, average density, and GPI puff timing. Values are taken at the time of the gas puff.

Shot	B_T [T]	I_p [MA]	P_{NBI} [MW]	$\langle n \rangle$ [cm ⁻³]	t_{GPI} [s]
138 845	0.34	0.8	3.8	5.9×10^{13}	0.58
138 846	0.34	0.8	3.8	5.9×10^{13}	0.58
138 847	0.33	0.8	3.8	6.0×10^{13}	0.58
141 249	0.36	0.7	2.9	3.3×10^{13}	0.48
141 254	0.37	0.8	2.9	3.4×10^{13}	0.48

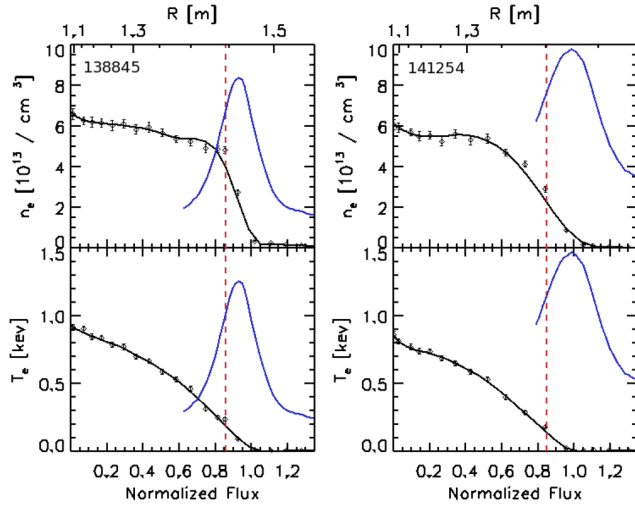


FIG. 2. Comparison of Thomson scattering profiles of n_e and T_e with GPI emission profile (blue curve) and $R = 140$ cm BES radial array channel used for comparison (red dashed line).

The physical distance between these two points is ~ 35 cm, and the distance along the generalized poloidal direction from the GPI corner to the intersection with the field line passing through this BES channel is ~ 20 cm. The comparisons presented in Secs. III and IV use the BES channel at the intersection of the radial and inner poloidal array as reference for shots 141 249 and 141 254. In R and Z, this channel is located just inside of the inner edge of the GPI view ~ 2 cm above the bottom of the GPI view. For shots 138 845–138 847, the BES channel one channel inside from the intersection of the radial array with the outer poloidal array is used for comparison. This channel lies ~ 4 cm out from the inner edge and ~ 1 cm above the bottom edge of the GPI view. GPI pixels used in comparisons are chosen to overlap in R and Z with the BES reference point to within 1 cm. This ensures that the comparison is done for similar flux surfaces, but field lines passing through the measurement locations are still separated by ~ 20 cm in the direction perpendicular to the magnetic field due to the toroidal separation. For the calculation of poloidal correlation lengths presented in Sec. V shots 141 249 and 141 254 use the BES inner poloidal array, and shots 138 845–138 847 use the outer BES poloidal array. GPI correlation lengths are calculated for poloidal separations about the center of the GPI view at the radial position of closest flux surface overlap with the given BES poloidal array.

III. FLUCTUATION STATISTICS

The BES light emission is subject to low-frequency, < 4 kHz, fluctuations in the neutral heating beams. In the analysis presented in this section, we account for this slow oscillation by applying a Gaussian convolution filter (GCF) with a 4 kHz e^{-1} frequency cutoff to time series of both diagnostics. This filter is strictly positive-valued in the time domain, which ensures that the resulting RMS fluctuations are real-valued at all times. Thus, we define a slowly varying “mean” intensity, $\langle I \rangle$ as the GCF of the raw trace, and the

fluctuating signal is defined as $\delta I = I - \langle I \rangle$. Following these definitions, the RMS fluctuation level is given by

$$\delta I_{rms} / \langle I \rangle = \frac{\langle (I - \langle I \rangle)^2 \rangle^{1/2}}{\langle I \rangle}, \quad (1)$$

where $\langle \cdot \rangle$ represents the GCF with 4 kHz frequency cutoff. Time traces of raw (I), mean ($\langle I \rangle$), and fluctuating (δI) intensity for both GPI and BES are plotted in Fig. 3. GPI RMS fluctuation levels are plotted in Fig. 4. GPI RMS fluctuation levels are $\sim 18\%$ of the mean which is ~ 9 times greater than the BES values of $\sim 2\%$ at this location. This result is consistent across all shots in the database used for this study. Near the separatrix, GPI δI values rise to $\sim 30\%$, and BES values rise to $\sim 5\%$ for these shots.

The dependence of GPI emission on the plasma parameters can be characterized as $I_{GPI} \propto n_e^\alpha T_e^\beta$, and α and β are tabulated for given values of n_e and T_e .³⁵ Near the 0.85 normalized flux position, the plasma conditions are $n_e = 2 - 5 \times 10^{13} \text{ cm}^{-3}$ and $T_e = 100 - 200 \text{ eV}$. Under these conditions, GPI exponents are $\alpha = 0.7 - 0.6$ and $\beta = 0.12 - 0.03$; thus for small fluctuations, the density dependence is at least 5 times stronger than the temperature dependence. Similarly, BES emission varies with plasma density to the $0.6 - 0.5$ power, and temperature dependence of the emission is typically negligible. Therefore, it is expected that both diagnostics predominantly measure density fluctuations, and, for small fluctuations, the ratio of GPI to BES RMS fluctuation levels normalized to mean is expected to be ~ 1.2 . The large discrepancy observed in fluctuation levels is well above the expected ratio of 1.2.

Further information on the fluctuation statistics is provided by the probability density functions (PDFs) of intensity fluctuations plotted in 5. PDFs are calculated for ~ 10 ms time blocks of intensity fluctuations at $r - r_{sep} \approx -2.9$ cm that have been high-pass filtered at 4 kHz. Fluctuation PDFs and their moments provide a well defined and experimentally accessible way of characterizing turbulence. Much effort in the study of turbulence has focused on the understanding and

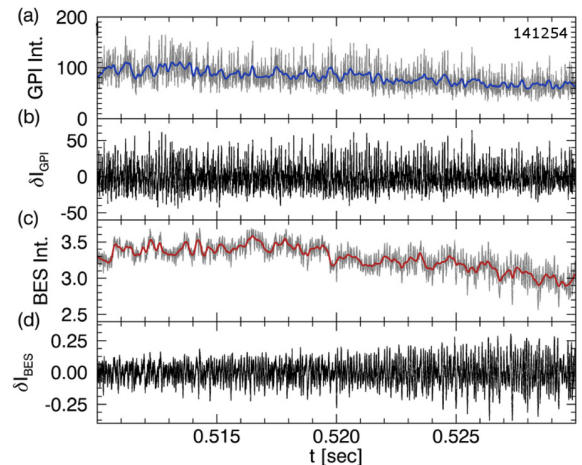


FIG. 3. Traces of (a) GPI raw (gray) and $\langle I \rangle$ (blue) and (b) δI . Plots (c) and (d) are BES traces. All traces taken at the 0.85 Ψ_N location. GPI gas puff begins at $t = 0.48$, and GPI light emission peaks at $t = 0.51$.

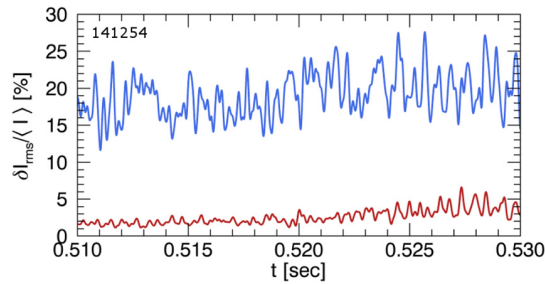


FIG. 4. Traces of $\delta I_{RMS}/\langle I \rangle$ for BES (red) and GPI (blue) for $\Psi_N = 0.85$.

prediction of the PDFs of turbulent quantities and the search for a universal distribution or universal features of turbulent distributions (for a review of the statistical description of plasmas, see Ref. 45). Furthermore, observations of non-Gaussian statistics and intermittency have led to a number of realizations about the importance of coherent structures and the nature of turbulent transport in the edge and SOL regions (e.g., Refs. 10, 46, and 47).

The PDFs and their normalized skewness (3rd moment) and normalized excess kurtosis values (4th moment) are shown in Figs. 5(a) and 5(b). Moments are normalized to the relevant power of the variance, and the normalized excess kurtosis is the difference of the normalized 4th moment of the PDF from Gaussian statistics. Information about first two moments of the PDF is captured by $\delta I_{rms}/\langle I \rangle$ as seen in Fig. 4. Skewness is a measure of the asymmetry of a distribution, while kurtosis is a measure of the relative weight of the tails. Deviations from a Gaussian PDF (represented by the dashed line in Fig. 5) are indicated by deviations of the normalized skewness from $S=0$ and the normalized excess kurtosis from $K=0$. For this shot, the GPI distribution is slightly skewed toward positive values, and a small positive kurtosis indicates more weight is present in the tails relative to a normal distribution. The BES distribution has negligible skew and small positive kurtosis.

Near $r - r_{sep} \approx -2.9$ cm, both GPI and BES intensity may be approximated by $I \approx Cn_e^\alpha$, where $\alpha \approx 0.6$ for GPI and $\alpha \approx 0.5$ for BES. Therefore, it is expected that the measured PDFs would be similar at this location. Averaging values for five 10 ms time blocks taken from 0 – 50 ms after the GPI emission peak for each of the 5 shots yields GPI skewness of $S = 0.24 \pm 0.25$ and kurtosis of $K = 0.38 \pm 0.44$, and BES skewness of $S = -0.01 \pm 0.13$ and kurtosis of

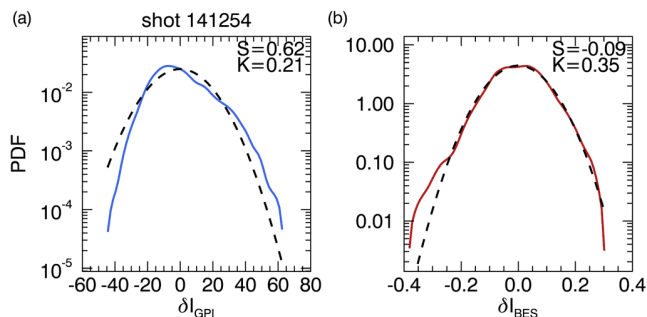


FIG. 5. PDFs of (a) GPI and (b) BES intensity from 10 ms period. Dashed Lines indicate Gaussian PDFs with similar mean and variance.

$K = 0.11 \pm 0.34$. Values are close to a normal distribution within variances for both diagnostics, but GPI does show a shift in the average values toward small positive skewness and kurtosis. Raising a random variable with a skewed distribution to a fractional power will shift the skew to negative values though, so it is possible that small differences could be explained by the difference in dependence on plasma parameters.

IV. CROSS-DIAGNOSTIC ANALYSIS

As discussed in Sec. III, both the GPI and BES diagnostics should predominantly measure density fluctuations near the 0.85 normalized flux position. In this section, we employ cross-correlation and cross-spectral analysis to estimate the similarity between time traces and spectral content of the signals. Due to technical issues with the BES data acquisition for these shots, there exists an unknown time offset between the GPI and BES time records, and, compounding this difficulty, a constant drift is present in the BES clock time kept by one diagnostic relative to the other. Fortunately, this drift is readily visible in the time-lagged cross-correlation function versus time, shown in Fig. 6, and can therefore be easily corrected. Here, correlations are calculated for ~ 3 ms time windows, and time traces have been high-pass filtered to removed the < 4 kHz fluctuations which are problematic due to beam fluctuations.

Finding the maximum correlation value for each time point yields a 1D function for the lag-time to peak correlation versus time. Then, a clock-correcting offset and dilation factor can be obtained by performing a linear fit of this function, and we utilized this dilation factor to align the BES time base with GPI in the analysis contained in this section. Note that this peak correlation value is persistent in time, and that the peak correlation value of $R \approx 0.5$ is significantly above the random level of $R \approx 0.2$ in this case.

An unresolved absolute time offset between the two signals still exists, and this offset limits the potential use of the correlation analysis in some applications. A simple estimate

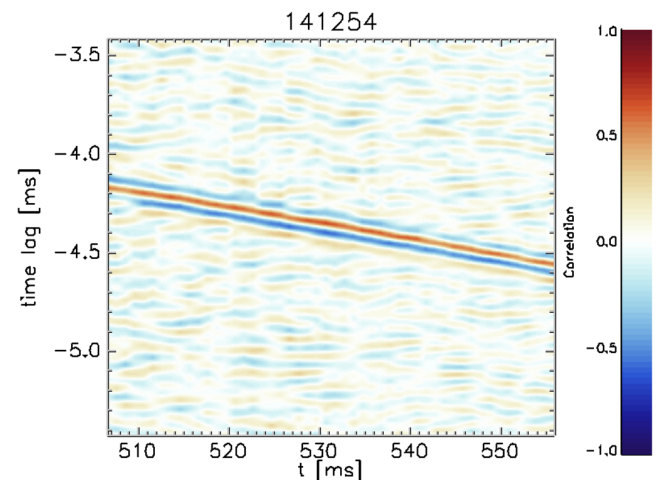


FIG. 6. Contour plot of time-lagged cross-correlation between GPI and BES signals versus time. Peak correlation value persists in time, but constant linear drift is present.

of the propagation time between diagnostic views predicts a time offset of 0.1 ms for the observed velocities presented in Sec. V. The analysis presented in the other sections of the paper is primarily statistical, and averages over several milliseconds up to 10 s of milliseconds. The analysis is performed separately on the BES and GPI data, and then the results are compared. The results are generally robust to small changes in the relative time offset.

With the correction applied to the BES time base, Fig. 7(a) shows the traces of time-lagged cross-correlation, and time traces of intensity fluctuations for a GPI pixel and a BES channel normalized to standard deviations are compared in Fig. 7(b). For shots listed in Table I, peak correlation values often exceed $R=0.6$, and a high degree of similarity is visually apparent in traces of the normalized fluctuations. This value of correlation is quite high considering the physical separation of ~ 35 cm between the measurement locations.

The cross-correlation vs. radius for GPI pixels correlated with the BES channel at $\Psi_N \approx 0.85$ is plotted in Figs. 8(a) and 8(b), and contour plots of the time-lagged cross-correlation vs. radius are included in Figs. 8(c) and 8(d). The solid line in Figs. 8(a) and 8(b) represents the correlation versus radius at the time lag of max correlation, and the dotted-dashed line represents the maximum correlation versus radius. The x-axis for these plots is the difference of the radial location of the GPI pixels mapped to the midplane and the midplane outer separatrix radius. The $r - r_{sep}$ location for the BES reference channel is illustrated by the dashed red line. The radial array of pixels ~ 2 cm above the bottom of the GPI view is used for this comparison.

The correlation functions in Figures 8(a)–8(d) exhibit a number of interesting features. First, the cross-correlation features for all shots are significantly radially extended, and strong correlation exists up to ~ 4 cm into the SOL. Second, shots in the 141 254 series generally exhibit a roughly linear time shift in the peak correlation time vs. radius. This is most likely due to the radially extended wavefronts for this structure being tilted in the radial vs. poloidal plane. Shots in the 138 845 series exhibit distinctly different behavior. For these shots, the peak correlation time is roughly constant inside of $r - r_{sep} \approx -2$ cm. At $r - r_{sep} = -1$ cm, the maximum correlation values are slightly suppressed, and outside

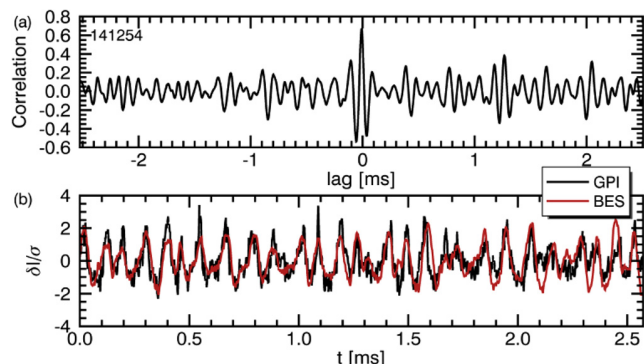


FIG. 7. Traces of (a) time-lagged cross-correlation between GPI and BES and (b) time traces of GPI and BES intensity.

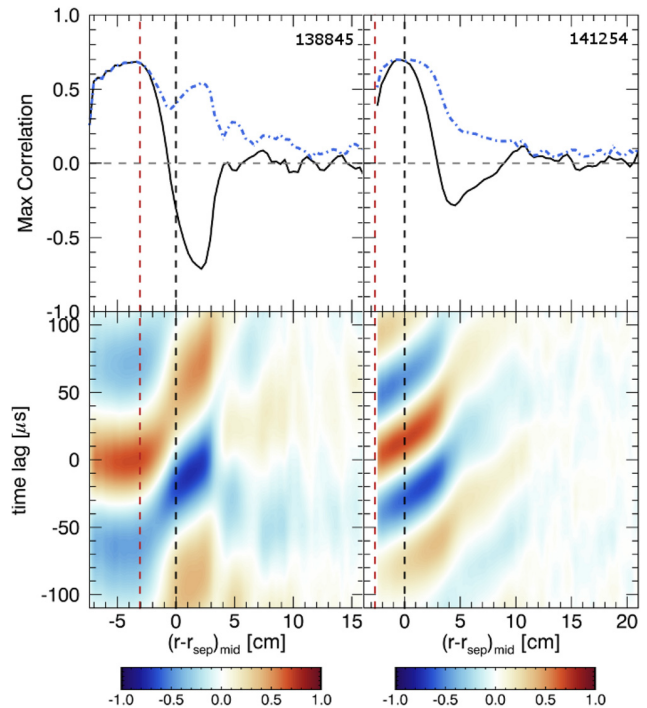


FIG. 8. (a) and (b) Plots of cross-correlation versus radius at time lag of maximum correlation (solid curves), and maximum cross-correlation versus radius (dotted-dashed curves). Plots (c) and (d) are contour plots of the cross-correlation vs. radius and time-lag. The black dashed line indicates the separatrix location, and the dashed red line indicates the radial location of the BES reference channel.

of this location a time shift or anti-correlation is observed. This may be indicative of a strong sheared flow present at $r - r_{sep} = -1$ cm. It should be noted, however, that the GPI light falls off rapidly inside of $r - r_{sep} \approx -4$ cm.

The cross-spectral density provides a measure of the shared frequency content between the BES and GPI signals. Traces of (a) cross-coherence, (b) cross-spectral density, (c) cross-phase, and (d) phase uncertainty comparing a BES channel and the closest GPI pixel in the R-Z plane are shown

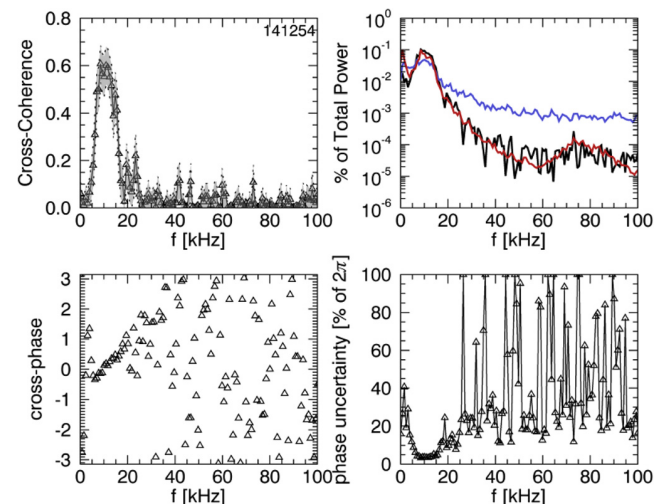


FIG. 9. Traces of (a) cross-coherence, (b) cross-spectral density, (c) cross-phase, and (d) phase uncertainty for the $\Psi_N \approx 0.85$ BES coord and the closest GPI pixel in the R-Z plane.

in Fig. 9. Similarities are seen for the low frequencies in the auto and cross spectral densities in Fig. 9(b), and a peak near 10 kHz is observed by both GPI and BES. The BES auto spectral density shows a second feature near 80 kHz that is not seen in the GPI spectrum. This 80 kHz feature is seen only in this shot, and it is likely hidden by noise in the GPI spectrum due to the higher noise floor.

Cross-coherence measures the constancy of the relative phase of similar frequency components between signals. The cross-coherence spectrum in Fig. 9(a) demonstrates that a well defined phase relationship exists between the two diagnostics for the 10 kHz frequency band, and similar peaks in the cross-coherence spectrum are seen in all shots in this study. The associated cross-phase $\phi_{xy} = 0 \pm 0.31$ is arbitrary due to the unresolved time offset between the two diagnostics. GPI observations show intensity fluctuations propagating downward ($-y$, ion diamagnetic drift direction) through the view, therefore the strong cross-coherence suggest that fluctuations, which are likely extended along field lines, propagate coherently between the GPI and BES views. This corresponds to a distance of ~ 20 cm in the generalized poloidal direction perpendicular to the magnetic field.

V. CHARACTERISTIC TIME AND LENGTH ESTIMATES

Estimates of the poloidal correlation length and the decorrelation time provide a characteristic length scale and a characteristic lifetime for the fluctuations, respectively. Aside from characterizing the fluctuations, the correlation lengths, decorrelation times, and scalings of these quantities

with other parameters may offer insight into the underlying instability driving the turbulence (e.g., see Refs. 6 and 48). We do not address the scaling here, but instead compare the estimates produced by the BES and GPI diagnostics. Auto-spectral density functions and cross-coherence functions between pixels separated by 2.4 cm, 4.8 cm, and 7.2 cm are plotted in Fig. 10. Peaks near 10 kHz and 80 kHz are present in the BES coherence spectrum, but only the 10 kHz peak is present in the GPI spectrum. This 80 kHz feature is only present in shot 141 254, but a strong coherence feature at low frequencies, between about 0–20 kHz, is present in all of the shots. This 80 kHz feature also does not show up in frequency spectra of the magnetic pick-up coils. For the following analysis, a band-pass filter is used with a low frequency cutoff of $f_{lc} = 4$ kHz and a high frequency cutoff of $f_{hc} = 50$ kHz. The low frequency cutoff is chosen to eliminate contamination of beam fluctuations in the BES signal, and the high frequency cutoff is placed at the point where the first coherence peak crosses the \sqrt{N} noise floor, where N is the number of time blocks used for the coherence calculation. This method of estimating decorrelation times is similar to the generalized cross-correlation method of time-delay estimation,⁴⁹ but an ad-hoc filter based on the coherence spectrum is used here.

After applying this filter, time-lagged cross-correlations are calculated using 4 ms long time blocks for varying pixel separations, and envelope functions are calculated using the Hilbert transform. Individual estimates of the correlation function are then averaged over 60 ms. Block-averaged correlation functions for GPI and BES are shown in Figs. 11(a)

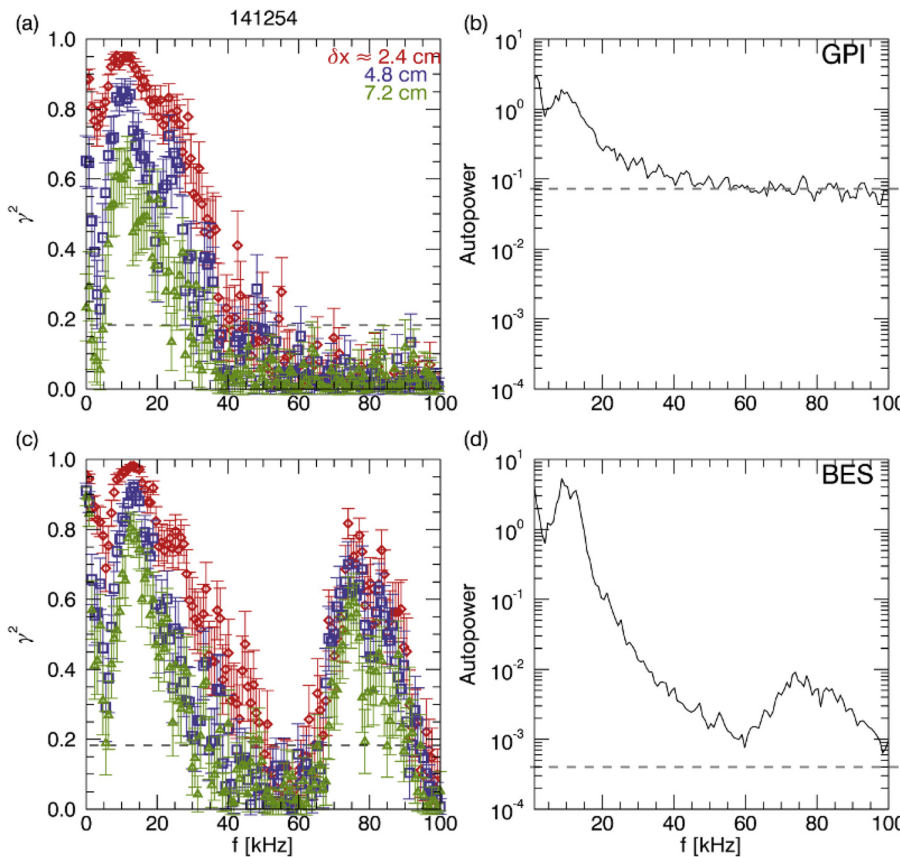


FIG. 10. Plots of the cross-coherence between poloidally separated channels for (a) GPI and (c) BES, and auto-power spectra for GPI (b) and BES (d).

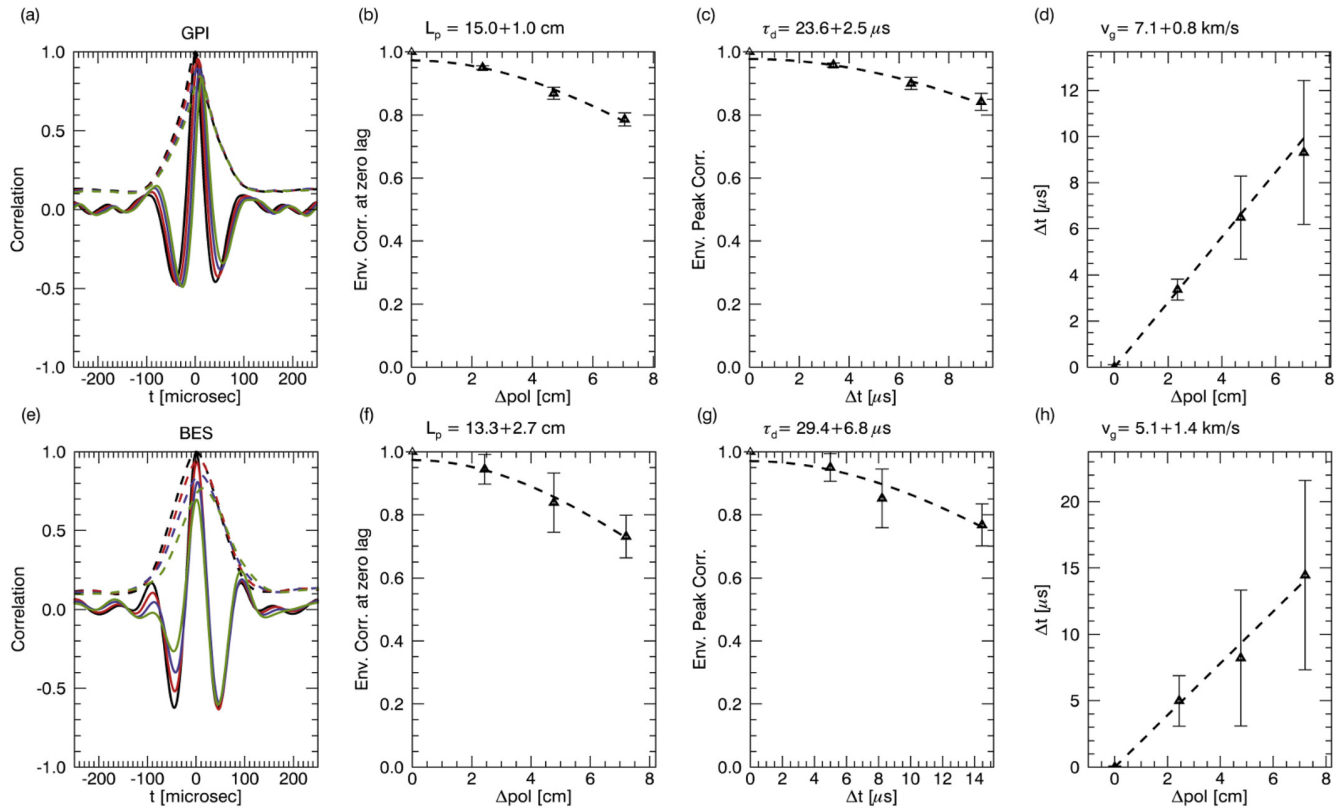


FIG. 11. Plots of (a) and (e) time-lagged cross-correlations (solid) with envelope functions (dashed), (b) and (f) zero-lag envelope peak correlation versus poloidal separation, (c) and (g) envelope peak correlation versus time-lag to peak, and (d) and (h) time-lag to envelope peak correlation versus poloidal separation. Values for poloidal correlation length and decorrelation time represent the $1/e$ length for a Gaussian fit to the corresponding plot.

and 11(e), respectively, and envelope functions calculated with the Hilbert transform are overlaid. Poloidal correlation lengths, L_{POL} , can be estimated by a Gaussian fit to the zero-lag envelope correlation versus pixel separation shown in Figs. 11(b) and 11(f). Similarly, decorrelation times, τ_c , can be estimated by a Gaussian fit to the envelope peak correlation versus time to peak correlation shown in Figs. 11(c) and 11(g). Finally, a statistical Time-Delay Estimation (TDE) velocity, v_g , may be estimated from the plot of the time to peak correlation versus poloidal separation shown in Figs. 11(d) and 11(h). This is a statistical velocity in the sense that the correlation functions have been averaged over tens of milliseconds. Structures are observed to propagate downward ($-y$, ion diamagnetic drift direction) in the GPI view, and the magnitude of the TDE velocity is estimated from Figs. 11(d) and 11(h).

Agreement between the estimated quantities for the shot shown in Fig. 11 is quite good. Expressing the agreement in terms of the percentage difference gives $12 \pm 14\%$ for L_{POL} , $22 \pm 19\%$ for τ_c , and $33 \pm 27\%$ for v_g . All values are less than or equal to 33% indicating agreement at the 33% level, and all values are consistent with zero well within two sigma.

Estimates of poloidal correlation lengths, decorrelation times, and statistical velocities for several shots are compared in Figs. 12(a)–12(c). Dashed lines in Fig. 12 indicate perfect agreement and $\pm 40\%$ deviations from that. All values show good agreement at the $\pm 40\%$ level, though BES velocity estimates derived from the correlation functions are

consistently lower than GPI velocities. Both diagnostics are aligned at 37° with respect to horizontal, and poloidal arrays of GPI and BES are aligned with the local poloidal direction from equilibrium reconstruction to within 15° . So the systematically lower velocity estimates should not be a consequence of the orientation of the diagnostic views. All velocities are in the ion diamagnetic drift direction ($-y$ in the GPI view).

VI. GAS PUFF EFFECTS

The peak neutral influx rate of the GPI diagnostic is 6.6×10^{21} atoms/s, and roughly $\sim 4 \times 10^{20}$ neutral deuterium atoms are puffed into the edge in total.⁵⁰ The total electron content of the plasma before the GPI puff is $\sim 6 \times 10^{20}$ electrons. It is estimated that $\sim 20\%$ (8×10^{19}) of the gas puff atoms become ionized inside the separatrix, but due to losses by edge particle diffusion the global density increase is expected to be $\leq 3\%$.⁵⁰ Previous work⁵⁰ has explored the possible perturbing effects of the GPI gas puff on the edge plasma and turbulence, and found that edge electron density and temperature changed by $\leq 10\%$ at the Thomson scattering location far from the GPI puff preceding and up to the peak in the GPI emission. Furthermore, edge turbulence quantities as measured by the GPI diagnostic did not show significant variation during the gas puff. Still, the effect of the gas puff on the local density and temperature in the gas cloud could not be measured directly. A cursory look at the BES measurements was included in the previous study, and

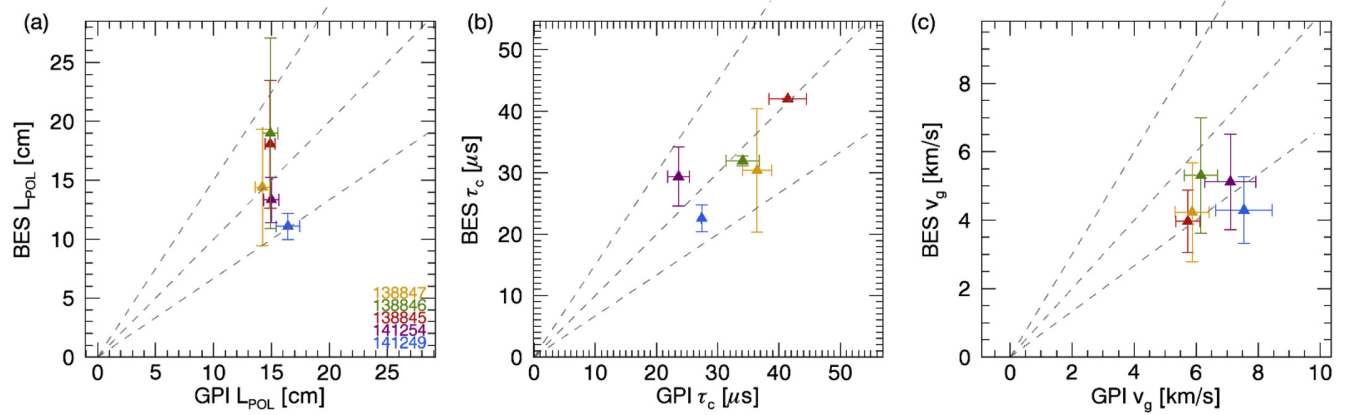


FIG. 12. Scatterplots comparing (a) poloidal correlation lengths estimates, (b) decorrelation time estimates, and (c) TDE velocity estimates.

it was found that the mean BES D_α emission increased and closely followed the GPI D_α emission during the GPI puff. Here we provide a more detailed examination of the GPI puff effects on the BES fluctuation spectra and poloidal correlation length.

The close proximity (~ 35 cm) of the BES sightlines to the GPI gas cloud provides us with an opportunity to examine the local effects of the gas cloud on the edge turbulence as measured by BES. The low-pass filtered, mean BES intensity is seen to increase concurrently with the GPI gas puff, and the increase at different radial and poloidal locations is captured by Fig. 13. The largest increase is seen at $X_{sep} = r - r_{sep} = -0.8$ cm and $Z = 7.6$ which corresponds to the bottom of the GPI view. Data from BES channels above $Z = 7.6$, closer to the center of the gas puff, is not available in these shots. The increase in signal decays at locations further from the gas cloud (decreasing R and Z), and typically the effect of the gas puff on the mean BES signal is negligible inside of $X_{sep} \approx -12$ cm.

The effect of the gas puff on the fluctuations is illustrated by Figs. 14(a) and 14(b) which show Continuous Wavelet Transforms (CWT) for $\delta I/I$, the BES fluctuations normalized to the 200 Hz low-pass filtered trace. The white line in Fig. 14(b) is the cone of influence, below which the wavelet coefficients are susceptible to edge effects. Time traces of frame-averaged GPI emission are plotted above the CWT. The low-pass filter is used to capture only the slow variation due to the GPI puff. Beam fluctuations manifest as a coherent feature near 900 Hz in both figures, and weaker,

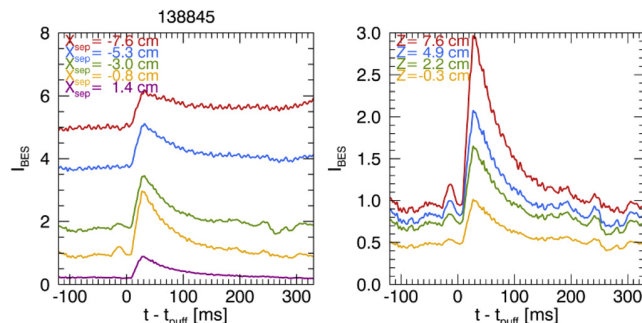


FIG. 13. Time traces of low-pass filtered BES intensity for varying (a) $X_{sep} = r - r_{sep}$ and (b) Z . Times are relative to the GPI gas puff timing.

less coherent harmonics can be observed up to ~ 4 kHz in average spectra for long time blocks. In Fig. 14(a), the amplitude of the 1–20 kHz fluctuation band increases with the GPI gas puff. Shots 138 845–138 847 each share this behavior, but no clear increase is visible in shots 141 249 and 141 254. In a previous study on gas puff effects,⁵⁰ Gas puffing in shot 138 845 was found to have the larger impact on edge density and temperature as measured by Thomson scattering than in other shots studied.

Block-averaged BES frequency spectra for $\delta I/I$ before and during the gas puff, plotted in Figs. 15(a) and 15(c), illustrate this increase in fluctuations more clearly. Here, autospectral power estimates are obtained by averaging spectra from 23 time blocks ~ 2.6 ms in length. Time blocks are taken at 60–0 ms before, and 30–90 ms following the opening of the gas puff valve. Fluctuations in the 1–10 kHz band increase significantly during the gas puff for Shots 138 845–138 847, and a smaller increase is seen only below ~ 4 kHz in Shots 141 249 and 141 254. Coherence spectra (using raw traces without normalization) for BES channels separated by 4.8 cm in the poloidal direction are plotted in Figs. 15(b) and 15(d). Before the gas puff, a strong coherence peak is seen between 10 and 20 kHz for shots 138 845–138 847, and during the gas puff the coherence values for this feature are reduced by ~ 0.2 . In contrast, Shots 141 249 and 141 254 show only minor changes in the coherence spectrum with the gas puffing, and the feature near 10 kHz appears to shift to slightly higher frequency.

Poloidal correlation lengths offer another tool to assess possible effects of the GPI gas puff on the BES signal. Correlation lengths are estimated by the same method used in Sec. V for 60–0 ms preceding, and 30–90 ms following the gas puff trigger. The results are tabulated in Table II. Poloidal correlation lengths for all shots become shorter during the gas puff, but difference values for only two shots are different from zero within uncertainties. One of these shots, 141 249, did not show a significant change in the BES frequency spectrum as seen in Fig. 15.

VII. DISCUSSION

The results presented above show that there are many similarities between the two diagnostics. Fluctuations are

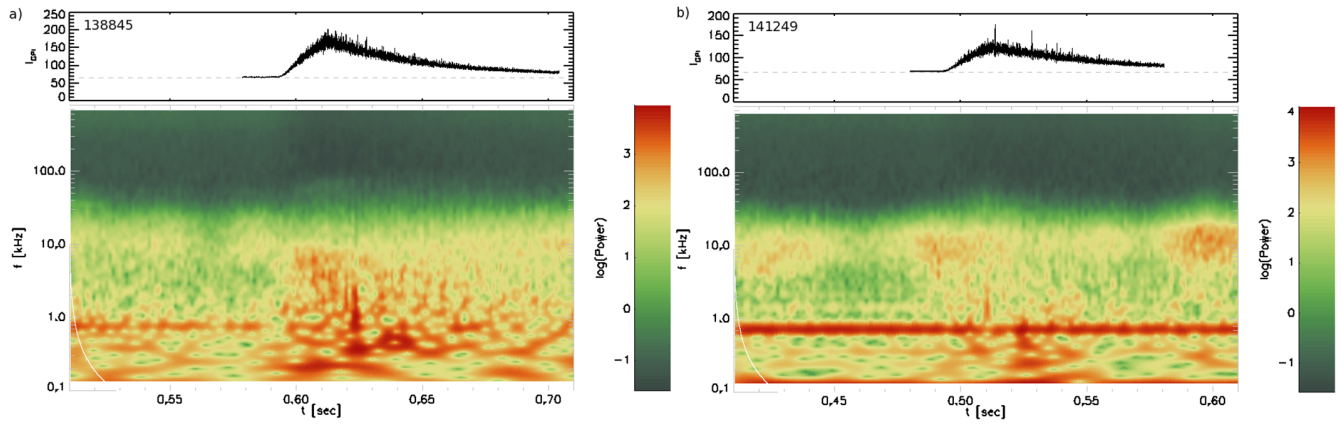


FIG. 14. Continuous wavelet transforms of BES fluctuations normalized to 200 Hz low-pass filter for shots 138 845 (a) and 141 249 (b). Time traces of the average GPI intensity are plotted above the CWTs.

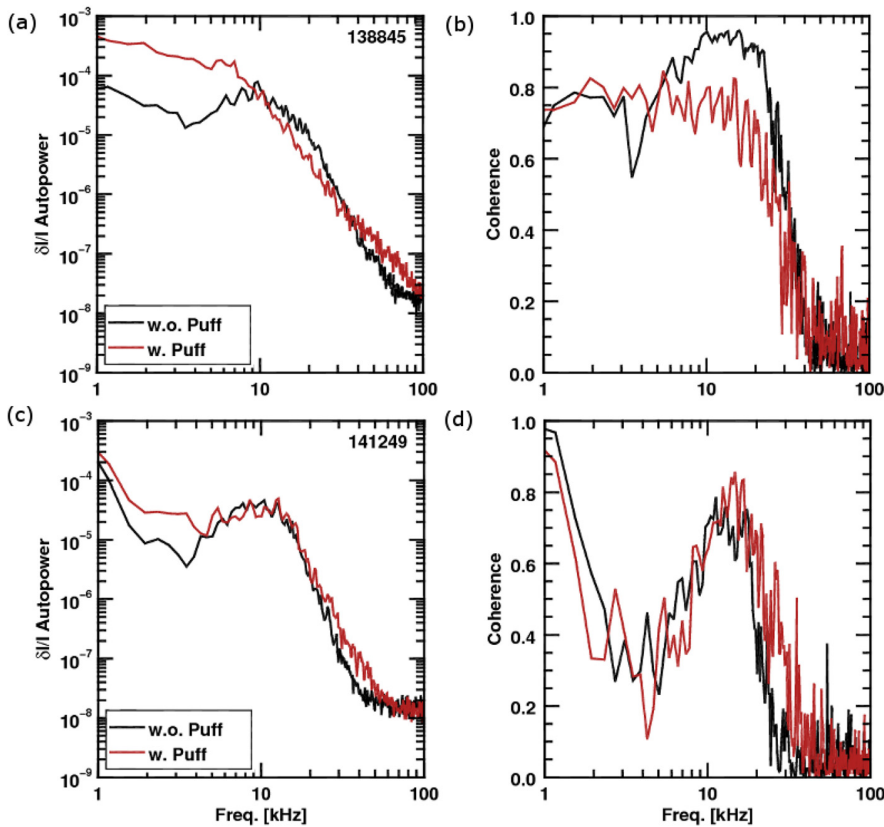


FIG. 15. (a) and (c) Block-averaged autopower spectra of fluctuations normalized to mean. (b) and (d) Coherence for BES channels separated by 4.8 cm. Black traces are spectra for 60–0 ms before the gas puff trigger, and red traces are spectra for 30–90 ms following the opening of the gas puff valve.

well correlated between diagnostics, and similar coherence peaks are seen near 10 kHz in the spectra of both diagnostics. Fluctuation PDFs of both diagnostics tend toward a Gaussian distribution ~ 3 cm inside the separatrix, where both

TABLE II. Poloidal correlation length estimates from 60–0 ms before and 30–90 ms after the gas puff trigger.

Shot	L_{POL} pre-puff [cm]	L_{POL} post-puff [cm]	Diff. [cm]
138 845	19.7 ± 3.3	17.7 ± 4.6	-2.0 ± 5.7
138 846	20.5 ± 2.6	17.3 ± 6.7	-3.1 ± 7.2
138 847	19.5 ± 2.6	13.3 ± 3.5	-6.2 ± 4.3
141 249	16.2 ± 2.6	10.5 ± 1.1	-5.6 ± 2.8
141 254	14.5 ± 1.0	13.2 ± 1.8	-1.4 ± 2.1

diagnostics are expected to predominantly measure density fluctuations. Finally, estimations of characteristic turbulence length and time scales are found to be in agreement at the 40% level.

Still, some discrepancies are found, and further discussion of the results and these discrepancies is presented in this section. Specifically, the large discrepancy in the normalized RMS fluctuation levels, and the large increase in BES signal during gas puffing warrant further discussion. In addition to these points, comments on alternative estimates of the poloidal correlation length and the nature of the dominant ~ 10 kHz feature are included in this section. Finally, the discussion concludes with some general comments on the relative benefits of both diagnostics.

A. Discrepancy in normalized RMS fluctuation level

The large discrepancy in RMS fluctuation levels suggests that either BES is underestimating, or GPI is overestimating the fluctuations at this location. Temperature dependence is not expected to be important, as discussed above, and both diagnostics have similar radial localization. The poloidal resolutions are different, which could lead to a difference in measured fluctuation levels due to an averaging over small scales, but applying a spatial filter to the GPI observations cannot account for the observed discrepancy. Reducing the GPI spatial resolution to that of BES by spatial filtering reduces the normalized fluctuation level from $19 \pm 3\%$ without filtering to $17 \pm 3\%$ with filtering. This is still much greater than BES estimate of $3 \pm 1\%$.

Large plasma fluctuations can lead to greater ionization of gas puff neutrals which will alter the neutral gas density in GPI gas cloud. For example, if the neutral gas cloud encounters an area of large fluctuations as it diffuses into the plasma from the gas source located at the edge of the device, then these fluctuations can be imprinted on the neutral gas density. These fluctuations are then carried with the neutral cloud as it continues to diffuse into the plasma edge, and the result is an observed fluctuation in GPI light due to a neutral density perturbation caused by plasma fluctuations existing between the emission region and the gas source. This effect is commonly referred to as “shadowing,” and a simple discussion of the effect can be found in Ref. 35. Similar effects are known to occur with beam neutrals in BES.⁵¹ To account for the observed discrepancy, the neutral density perturbation at the measurement location would need to be of order 10%.

Degas 2 simulations have been performed to provide a rough estimate of the effects of neutral density perturbations. Two test cases are created from the experimental Thomson scattering plasma profiles for shot 138 846. The plasma profiles for case (+) have been uniformly multiplied by a factor of 1.25, and for case (−) the profiles have been uniformly divided by a factor of 1.25. At radii inside of the location of peak GPI emission, the ratio of neutral density in case (+) to case (−) is ~ 0.4 meaning that an increase in plasma parameters depletes neutrals inside of the peak in GPI emission, as one would expect. Furthermore, the effect is quite large, and results in a ratio of D_α light emitted at these locations in case (+) to case (−) of ~ 0.5 . So the decrease in emission due to fewer neutral atoms dominates the expected increase in emission from the increase in density and temperature. This would suggest that neutral density perturbations can have a significant effect on the normalized fluctuation levels.

If neutral density perturbations were the dominant cause of fluctuations inside of the GPI emission peak, then one would expect that the GPI fluctuations at this location to be anti-correlated with fluctuations outside of this location (hotter, denser, brighter perturbations near the separatrix reduce D_α emission inside). This is seen, for example, in Fig. 8, but it is not clear how to separate this effect from a physical radial wavelength. Also, several diagnostics have shown that plasma fluctuations near the separatrix and in the near SOL are positively skewed. This leads one to expect that if neutral density perturbations are dominant inside of the emission

peak, then the skewness of these fluctuations should be negative. This is not what is found in Fig. 5. The shadowing effect is a complicated process involving full 3D plus time dynamics, and a dedicated experimental and numerical effort is likely required to fully understand it.

Langmuir probe measurements could help resolve this discrepancy. Previous studies found edge turbulence measurements made by Langmuir probes to be similar to BES measurements⁵² and measurements of visible emission from the plasma edge,⁵³ but a direct comparison of GPI, BES, and probes has not been performed on NSTX. The NSTX fast scanning probe diagnostic⁵⁴ was used during this run campaign, and it is capable of making measurements of edge fluctuations in NSTX H-mode plasmas for $\psi_N > 0.9$. A study of edge turbulence in NSTX during Type-III ELMing H-mode plasmas has been published recently,⁵⁵ but the shots used were significantly different from those used in this paper. Unfortunately, no overlapping GPI and probe data exist for the shots used in this study. There are additional diagnostic subtleties that complicate a direct comparison. For example, probe measurements are possible only in the region of the plasma where temperature fluctuations are believed to have an important impact on GPI measurements. For these reasons, a comparison of GPI and probe measurements is not addressed here.

B. Increase in BES signal during gas puffing

The large, $\sim 300\%$ increase in BES mean intensity levels during the gas puffing is a striking feature of the analysis in Sec. VI. To better understand the effects of the gas puff on the BES measurements, DEGAS 2 simulations³⁸ have been performed, and it is found that gas puffing increases the neutral deuterium content at the intersection of the BES view with the neutral beams by $\sim 10^{17}/\text{m}^3$. This is 2 orders of magnitude less than the plasma density at this location; therefore, it is not expected that beam neutral–thermal neutral collisions will play a significant role. Furthermore, the increase in local plasma density is presumably of this order or less, so it is unlikely that the increased emission is attributable to an increased plasma density.

The gas puff does lead to an increase in D_α signal on the BES channels, but the BES system is designed to use the Doppler shift and interference filters to reject most of this background emission. The DEGAS 2 Simulations estimate the thermal D_α signal on the BES channels to be $\leq 6.6 \times 10^{19}$ photons/(m^2 sr s). The BES étendue is 2.3 mm^2 sr, optical fiber losses are 42%, and attenuation by the interference filter is $5 \times 10^{-4}\%$ at the unshifted D_α wavelength. Thus BES is expected to measure 3.2×10^6 photons/s, or a $65 \mu\text{V}$ signal output. This is several orders of magnitude less than the $\sim 1 \text{ V}$ signal levels typically seen, and clearly does not account for the increase seen in the mean BES signal. The source of the BES signal increase with GPI gas puffing is still not understood.

C. Alternative estimates of the poloidal correlation length

Poloidal correlation length estimates have also been performed using the full extent of the GPI view, and this method

is able to resolve the first anti-node of the spatial correlation function. The results of the calculation using the full view strongly suggest that the 4-point estimate used in Figs. 11 and 12 significantly underestimates the correlation length. During the 2010 run campaign, it was discovered that BES poloidal arrays did not have the poloidal coverage to resolve the first anti-node, and, due to data acquisition constraints, only 4-channels of the BES poloidal array were typically available. Therefore, the 4-point estimate is used for comparison here, and this estimate does appear to be consistent between the two diagnostics. The upgraded BES view for NSTX-U has been designed to address this issue, and should be able to resolve anti-nodes of the correlation function.

D. Nature of the ~ 10 kHz fluctuations

Each of the shots in the database studied here exhibits a feature in the cross-diagnostic coherence spectrum near 10 kHz. The full width at half maximum for the feature is between 3 and 5 kHz. The CWT of BES data (Fig. 14) indicates that this feature is incoherent, and appears as a collection of intermittent bursts of power between 5 and 15 kHz. This can be contrasted with the behavior of the persistent, coherent 900 Hz beam fluctuation. In the GPI view, this feature is characterized by spatially localized intensity structures, or intensity pulses, that appear quasi-periodically and travel through the view from top to bottom (in the Ion Diamagnetic Drift Direction). To the extent that this mode is dominant in each of the shots, the analysis presented here (fluctuation statistics, poloidal correlation lengths, etc.) is a characterization of this feature. Presently, the nature of these fluctuations is not well understood, but the analysis presented here can offer some simple characterization. The GPI correlation lengths calculated using the full GPI poloidal extent indicate the characteristic size for this feature is between 20 and 30 cm for shots 138 845–138 847 and 30 and 40 cm for shots 141 249 and 141 254. Estimates of the dominant poloidal wavelength determined by the distance between the correlation peak and the first anti-node of the poloidal correlation function yield $k_{\perp}\rho_s \approx 0.1 - 0.2$. The correlation versus radius plots of Fig. 8 suggest that these structures are radially extended, and they are present several centimeters into the SOL. Detailed analysis of the low-wavenumber turbulence in NSTX H-modes seen by BES can be found in Refs. 6 and 48.

E. General comments on the comparison of GPI and BES

Given the similarities between these two diagnostic approaches, it is tempting to ask the seemingly simple question: Which diagnostic is better, or which is “correct”? It is important to recognize, however, that both diagnostics have their own strengths, and are in many ways complementary. The Phantom v710 cameras and optics used for the NSTX GPI system provides an unmatched combination of high spatial resolution ($k_{\theta}\rho_s \lesssim 2$), high time resolution (400 kHz sampling rate), spatial coverage, and a high pixel count (64×80) for measuring the plasma edge. Furthermore, detailed 2-D imaging is valuable in the creation of a self-consistent explanations of physical phenomena (e.g., imaging blobs

with GPI,^{19,40} ELM filaments with fast cameras,^{56,57} and Sawtooth pulses with Electron Cyclotron Emission Imaging (ECEI)⁵⁸). GPI is limited, however, by the penetration of the neutral gas into the plasma, thus measurements can only be made of the outer several centimeters of the plasma and the SOL. BES, on the other hand, is capable of making precise measurements of density fluctuations over much of the plasma radius with comparable spatial resolution, and high time resolution (200 MHz sampling rate). The NSTX BES system, however, does have limited 2-D coverage, and expanding the number of channels can be expensive. In addition, BES requires the operation of either neutral heating beams or specialized diagnostic neutral beams. In the end, the goal of both diagnostics is to validate turbulence simulations, and having data from both diagnostics provides more points of comparison.

VIII. SUMMARY

Comparisons of BES and GPI measurements of edge fluctuations in NSTX are presented in this paper. The BES and GPI diagnostic views share coverage over the range of normalized flux from $\Psi_N \geq 0.8$ into the SOL at similar poloidal angles, but are separated in toroidal angle by $\sim 16^\circ$. Near $\Psi_N = 0.85$ both diagnostics are expected to predominantly measure density fluctuations. The measured fluctuations are therefore expected to have similar characteristics, and many similarities are observed. Direct comparison of GPI and BES fluctuation measurements on field lines separated by ~ 20 cm in the direction perpendicular to B yields strong correlations, $R > 0.6$, and strong cross-coherence between ~ 5 and 15 kHz. Fluctuation PDFs and their moments show good agreement at $\Psi_N = 0.85$, and both GPI and BES distributions are close to Gaussian at this location. Correlation lengths, decorrelation times, and TDE velocity estimates all show good agreement within $\pm 40\%$. It should be emphasized that, given the physical separation of the measurement locations, the observed agreement is very strong.

There are some important differences, however. Measured GPI fluctuation levels normalized to the mean are a factor of $9 \times$ greater than the measured BES fluctuation levels. This discrepancy is unresolved, but could be explained by either an underestimate of the fluctuation level by BES at this location or an overestimate by GPI. It is possible that large fluctuations in the plasma density near the separatrix may induce fluctuations in the neutral density, thus an increased fluctuation level would be measured by GPI at smaller radii due to the modulated neutral density. In addition to the dissimilarity of fluctuation levels, differences in the fluctuation PDFs are present at larger radii, but this is not unexpected due to large-fluctuation amplitudes and increased temperature dependence of the light emission. Also, comparing the 4-point estimate of the correlation length to a calculation utilizing the full GPI spatial information revealed that the 4-point estimate consistently underestimates the poloidal correlation length.

Finally, effects of the neutral deuterium puff used for GPI on the BES mean and fluctuations are quantified. BES mean

intensity levels are seen to increase by as much as 300% near the separatrix position. Sensitivity of the BES mean to the neutral puff decreases with distance of the measurement location from the center of the gas cloud. In addition, CWTs and frequency spectra for fluctuations normalized to the 200 Hz low-pass filtered BES signal show an increase in relative fluctuation levels in the 1–10 kHz band, but only one shot shows a significant change in the poloidal correlation measured before and during the gas puff.

ACKNOWLEDGMENTS

The authors would like to acknowledge the NSTX Team, Rajesh Maingi for gas puffing during experiments, Ben LeBlanc for providing Thomson scattering data, and Ricky Maqueda. This work was supported by Department of Energy Grant Nos. DE-FG02-09ER54995, DE-SC0001966, and DE-AC02-09CH11466.

- ¹ASDEX Team, “The h-mode of ASDEX,” *Nucl. Fusion* **29**(11), 1959–2040 (1989).
- ²R. A. Moyer, K. H. Burrell, T. N. Carlstrom, S. Coda, R. W. Conn, E. J. Doyle, P. Gohil, R. J. Groebner, J. Kim, R. Lehmer, W. A. Peebles, M. Porkolab, C. L. Rettig, T. L. Rhodes, R. P. Seraydarian, R. Stockdale, D. M. Thomas, G. R. Tynan, and J. G. Watkins, “Beyond paradigm—Turbulence, transport, and the origin of the radial electric-field in low to high confinement mode transitions in the DIII-D tokamak,” *Phys. Plasmas* **2**(6), 2397–2407 (1995).
- ³G. R. Tynan, L. Schmidt, L. Blush, J. A. Boedo, R. W. Conn, R. Doerner, R. Lehmer, R. Moyer, H. Kugel, R. Bell, S. Kaye, M. Okabayashi, S. Sesnic, and Y. Sun, “Turbulent edge transport in the Princeton beta-experiment-modified high confinement mode,” *Phys. Plasmas* **1**(10), 3301–3307 (1994).
- ⁴G. Federici, A. Loarte, and G. Strohmayer, “Assessment of erosion of the ITER divertor targets during type I ELMS,” *Plasma Phys. Controlled Fusion* **45**(9), 1523–1547 (2003).
- ⁵S. F. Paul, N. Bretz, R. D. Durst, R. J. Fonck, Y. J. Kim, E. Mazzucato, and R. Nazikian, “Measurements of long-wavelength density-fluctuations in TFTR,” *Phys. Fluids B* **4**(9), 2922–2928 (1992).
- ⁶D. R. Smith, R. J. Fonck, G. R. McKee, D. S. Thompson, R. E. Bell, A. Diallo, W. Guttenfelder, S. M. Kaye, B. P. LeBlanc, and M. Podesta, “Characterization and parametric dependencies of low wavenumber pedestal turbulence in the national spherical torus experiment,” *Phys. Plasmas* **20**(5), 055903 (2013).
- ⁷M. Jakubowski, R. J. Fonck, and G. R. McKee, “Observation of coherent sheared turbulence flows in the DIII-D tokamak,” *Phys. Rev. Lett.* **89**(26), 265003 (2002).
- ⁸G. R. McKee, R. J. Fonck, M. Jakubowski, K. H. Burrell, K. Hallatschek, R. A. Moyer, D. L. Rudakov, W. Nevins, G. D. Porter, P. Schoch, and X. Xu, “Experimental characterization of coherent, radially-sheared zonal flows in the DIII-D tokamak,” *Phys. Plasmas* **10**(5), 1712–1719 (2003); in *44th Annual Meeting of the Division of Plasma of the American-Physical-Society, Orlando, Florida*, November 11–15, 2002 (Division of Plasma Physics, American Physical Society).
- ⁹G. R. McKee, D. K. Gupta, R. J. Fonck, D. J. Schlossberg, M. W. Shafer, and P. Gohil, “Structure and scaling properties of the geodesic acoustic mode,” *Plasma Phys. Controlled Fusion* **48**(4), S123–S136 (2006).
- ¹⁰J. A. Boedo, D. L. Rudakov, R. A. Moyer, G. R. McKee, R. J. Colchin, M. J. Schaffer, P. G. Stangeby, W. P. West, S. L. Allen, T. E. Evans, R. J. Fonck, E. M. Hollmann, S. Krasheninnikov, A. W. Leonard, W. Nevins, M. A. Mahdavi, G. D. Porter, G. R. Tynan, D. G. Whyte, and X. Xu, “Transport by intermittency in the boundary of the DIII-D tokamak,” *Phys. Plasmas* **10**(5), 1670–1677 (2003); in *44th Annual Meeting of the Division of Plasma of the American-Physical-Society, Orlando, Florida*, November 11–15, 2002 (Division of Plasma Physics, American Physical Society).
- ¹¹R. J. Maqueda, G. A. Wurden, S. Zweben, L. Roquemore, H. Kugel, D. Johnson, S. Kaye, S. Sabbagh, and R. Maingi, “Edge turbulence measurements in NSTX by gas puff imaging,” *Rev. Sci. Instrum.* **72**(1), 931–934 (2001); in *13th Topical Conference on High-Temperature Plasma Diagnostics, Tucson, Arizona*, June 18–22, 2000 (Physics Division, Los Alamos National Laboratory; Inertial Confinement Fusion and Radiation Physics Program, Los Alamos National Laboratory; General Atomics; Division of Plasma Physics, American Physical Society; Office of Fusion Energy Sciences, U.S. DOE; Office of Defense Sciences, U.S. DOE).
- ¹²S. J. Zweben, D. P. Stotler, J. L. Terry, B. LaBombard, M. Greenwald, M. Muterspaugh, C. S. Pitcher, K. Hallatschek, R. J. Maqueda, B. Rogers, J. L. Lowrance, V. J. Mastrocola, G. F. Renda, and C. M. G. Alcator, “Edge turbulence imaging in the Alcator C-Mod tokamak,” *Phys. Plasmas* **9**(5), 1981–1989 (2002); in *43rd Annual Meeting of the Division of Plasma Physics of the American-Physical-Society*, Long Beach, California, Oct. 29–Nov. 2, 2001 (Division of Plasma Physics, American Physical Society).
- ¹³I. Shesterikov, Y. Xu, M. Berte, P. Dumortier, M. Van Schoor, M. Vergote, B. Schweer, and G. Van Oost, “Development of the gas-puff imaging diagnostic in the TEXTOR tokamak,” *Rev. Sci. Instrum.* **84**(5), 053501 (2013).
- ¹⁴M. Agostini, R. Cavazzana, P. Scarin, and G. Serianni, “Operation of the gas-puff imaging diagnostic in the RFX-mod device,” *Rev. Sci. Instrum.* **77**(10), 10E513 (2006).
- ¹⁵S. C. Liu, L. M. Shao, S. J. Zweben, G. S. Xu, H. Y. Guo, B. Cao, H. Q. Wang, L. Wang, N. Yan, S. B. Xia, W. Zhang, R. Chen, L. Chen, S. Y. Ding, H. Xiong, Y. Zhao, B. N. Wan, X. Z. Gong, and X. Gao, “New dual gas puff imaging system with up-down symmetry on experimental advanced superconducting tokamak,” *Rev. Sci. Instrum.* **83**(12), 123506 (2012).
- ¹⁶M. Agostini, S. J. Zweben, R. Cavazzana, P. Scarin, G. Serianni, R. J. Maqueda, and D. P. Stotler, “Study of statistical properties of edge turbulence in the national spherical torus experiment with the gas puff imaging diagnostic,” *Phys. Plasmas* **14**(10), 102305 (2007).
- ¹⁷I. Cziegler, J. L. Terry, J. W. Hughes, and B. LaBombard, “Experimental studies of edge turbulence and confinement in Alcator C-Mod,” *Phys. Plasmas* **17**(5), 056120 (2010); in *51st Annual Meeting of the Division of Plasma-Physics of the American-Physics-Society*, Atlanta, GA, November 2–6, 2009 (Division of Plasma Physics, American Physical Society).
- ¹⁸R. Kube, O. E. Garcia, B. LaBombard, J. L. Terry, and S. J. Zweben, “Blob sizes and velocities in the Alcator C-Mod scrape-off layer,” *J. Nucl. Mater.* **438**, S505–S508 (2013); in *20th International Conference on Plasma-Surface Interactions in Controlled Fusion Devices (PSI)*, May 21–25, 2012 (Forschungszentrum Jülich, Aachen, Germany).
- ¹⁹J. R. Myra, D. A. D’Ippolito, D. P. Stotler, S. J. Zweben, B. P. LeBlanc, J. E. Menard, R. J. Maqueda, and J. Boedo, “Blob birth and transport in the tokamak edge plasma: Analysis of imaging data,” *Phys. Plasmas* **13**(9), 092509 (2006).
- ²⁰J. L. Terry, S. J. Zweben, O. Grulke, M. J. Greenwald, and B. LaBombard, “Velocity fields of edge/scrape-off-layer turbulence in Alcator C-Mod,” *J. Nucl. Mater.* **337**(1–3), 322–326 (2005); in *16th International Conference on Plasma Surface Interactions in Controlled Fusion Devices*, Portland, ME, May 24–28, 2004 (Plasma Science and Fusion Centre, MIT; U.S. DOE).
- ²¹T. Munsat and S. J. Zweben, “Derivation of time-dependent two-dimensional velocity field maps for plasma turbulence studies,” *Rev. Sci. Instrum.* **77**(10), 103501 (2006).
- ²²S. J. Zweben, R. J. Maqueda, R. Hager, K. Hallatschek, S. M. Kaye, T. Munsat, F. M. Poli, A. L. Roquemore, Y. Sechrest, and D. P. Stotler, “Quiet periods in edge turbulence preceding the L-H transition in the National Spherical Torus Experiment,” *Phys. Plasmas* **17**(10), 102502 (2010).
- ²³Y. Sechrest, T. Munsat, D. A. D’Ippolito, R. J. Maqueda, J. R. Myra, D. Russell, and S. J. Zweben, “Flow and shear behavior in the edge and scrape-off layer of L-mode plasmas in National Spherical Torus Experiment,” *Phys. Plasmas* **18**(1), 012502 (2011).
- ²⁴I. Cziegler, P. H. Diamond, N. Fedorczak, P. Manz, G. R. Tynan, M. Xu, R. M. Churchill, A. E. Hubbard, B. Lipschultz, J. M. Sierchio, J. L. Terry, and C. Theiler, “Fluctuating zonal flows in the I-mode regime in Alcator C-Mod,” *Phys. Plasmas* **20**(5), 055904 (2013).
- ²⁵R. J. Maqueda, R. Maingi, and NSTX Team, “Primary edge localized mode filament structure in the National Spherical Torus Experiment,” *Phys. Plasmas* **16**(5), 056117 (2009); in *50th Annual Meeting of the Division of Plasma Physics of the American-Physical-Society, Dallas, TX*, February 1, 2008 (Division of Plasma Physics, American Physical Society).
- ²⁶Y. Sechrest, T. Munsat, D. J. Battaglia, and S. J. Zweben, “Two-dimensional characterization of ELM precursors in NSTX,” *Nucl. Fusion* **52**(12), 123009 (2012).
- ²⁷G. S. Xu, L. M. Shao, S. C. Liu, H. Q. Wang, B. N. Wan, H. Y. Guo, P. H. Diamond, G. R. Tynan, M. Xu, S. J. Zweben, V. Naulin, A. H. Nielsen, J. J. Rasmussen, N. Fedorczak, P. Manz, K. Miki, N. Yan, R. Chen, B. Cao, L. Chen, L. Wang, W. Zhang, and X. Z. Gong, “Study of the L-I-H

- transition with a new dual gas puff imaging system in the east superconducting tokamak." *Nucl. Fusion* **54**(1), 013007 (2014).
- ²⁸R. K. Janev, C. D. Boley, and D. E. Post, "Penetration of energetic neutral beams into fusion plasmas," *Nucl. Fusion* **29**(12), 2125–2140 (1989).
- ²⁹C. D. Boley, R. K. Janev, and D. E. Post, "Enhancement of the neutral-beam stopping cross-section in fusion plasmas due to multistep collision processes," *Phys. Rev. Lett.* **52**(7), 534–537 (1984).
- ³⁰H. Anderson, M. G. von Hellermann, R. Hoekstra, L. D. Horton, A. C. Howman, R. W. T. Konig, R. Martin, R. E. Olson, and H. P. Summers, "Neutral beam stopping and emission in fusion plasmas I: Deuterium beams," *Plasma Phys. Controlled Fusion* **42**(7), 781–806 (2000).
- ³¹I. H. Hutchinson, "Excited-state populations in neutral beam emission," *Plasma Phys. Controlled Fusion* **44**(1), 71–82 (2002).
- ³²O. Marchuk, G. Bertschinger, W. Biel, E. Delabie, M. G. von Hellermann, R. Jaspers, and D. Reiter, "Review of atomic data needs for active charge-exchange spectroscopy on ITER," *Rev. Sci. Instrum.* **79**(10), 10F532 (2008); in 17th Topical Conference on High-Temperature Plasma Diagnostics, Albuquerque, NM, 2008.
- ³³S. Suzuki, T. Shirai, M. Nemoto, K. Tobita, H. Kubo, T. Sugie, A. Sakasai, and Y. Kusama, "Attenuation of high-energy neutral hydrogen beams in high-density plasmas," *Plasma Phys. Controlled Fusion* **40**(12), 2097–2111 (1998).
- ³⁴E. Delabie, M. Brix, C. Giroud, R. J. E. Jaspers, O. Marchuk, M. G. O'Mullane, Y. Ralchenko, E. Surrey, M. G. von Hellermann, K. D. Zastrow, and JE Contributors, "Consistency of atomic data for the interpretation of beam emission spectra," *Plasma Phys. Controlled Fusion* **52**(12), 125008 (2010).
- ³⁵D. P. Stotler, B. LaBombard, J. L. Terry, and S. J. Zweben, "Neutral transport simulations of gas puff imaging experiments," *J. Nucl. Mater.* **313**, 1066–1070 (2003); in 15th International Conference on Plasma-Surface Interactions in Controlled Fusion Devices (PSI-15), Gifu, Japan, May 26–31, 2002.
- ³⁶D. P. Stotler, D. A. D'Ippolito, B. LeBlanc, R. J. Maqueda, J. R. Myra, S. A. Sabbagh, and S. J. Zweben, "Three-dimensional neutral transport simulations of gas puff imaging experiments," *Contrib. Plasma Phys.* **44**(1–3), 294–300 (2004); in 9th International Workshop on Plasma Edge Theory in Fusion Devices, University of California, San Diego, San Diego, CA, September 3–5, 2003 (Engineering Department, UCSD; Lawrence Livermore National Laboratory; Office of Fusion Energy, Department of Energy; Max-Planck Institute of Plasma Physics).
- ³⁷D. P. Stotler, J. Boedo, B. LeBlanc, R. J. Maqueda, and S. J. Zweben, "Progress towards the validation of models of the behavior of neutral helium in gas puff imaging experiments," *J. Nucl. Mater.* **363**, 686–692 (2007); in 17th International Conference on Plasma-Surface Interactions in Controlled Fusion Devices, Hefei, Peoples Republic of China, May 22–26, 2006 (Institute of Plasma Physics; Bureau International Cooperation, Chinese Academy of Sciences; National Natural Science Foundation of China).
- ³⁸B. Cao, D. P. Stotler, S. J. Zweben, M. Bell, A. Diallo, and B. LeBlanc, "Comparison of gas puff imaging data in NSTX with DEGAS 2 simulations," *Fusion Sci. Technol.* **64**(1), 29–38 (2013).
- ³⁹R. J. Maqueda, G. A. Wurden, D. P. Stotler, S. J. Zweben, B. LaBombard, J. L. Terry, J. L. Lowrance, V. J. Mastrocola, G. F. Renda, D. A. D'Ippolito, J. R. Myra, and N. Nishino, "Gas puff imaging of edge turbulence (invited)," *Rev. Sci. Instrum.* **74**(3), 2020–2026 (2003); in 14th Topical Conference on High-Temperature Plasma Diagnostics, Madison, Wisconsin, July 8–11, 2002 (University of Wisconsin Madison; Division of Plasma Physics, American Physical Society; Office of Fusion Energy Sciences and Defense Sciences, U.S. DOE).
- ⁴⁰S. J. Zweben, R. J. Maqueda, D. P. Stotler, A. Keese, J. Boedo, C. E. Bush, S. M. Kaye, B. LeBlanc, J. L. Lowrance, V. J. Mastrocola, R. Maingi, N. Nishino, G. Renda, D. W. Swain, J. B. Wilgen, and NSTX Team, "High-speed imaging of edge turbulence in NSTX," *Nucl. Fusion* **44**(1), 134–153 (2004).
- ⁴¹G. R. Tynan, A. Fujisawa, and G. McKee, "A review of experimental drift turbulence studies," *Plasma Phys. Controlled Fusion* **51**(11), 113001 (2009).
- ⁴²R. J. Fonck, P. A. Duperrex, and S. F. Paul, "Plasma fluctuation measurements in tokamaks using beam-plasma interactions," *Rev. Sci. Instrum.* **61**(10), 3070 (1990).
- ⁴³D. R. Smith, H. Feder, R. Feder, R. J. Fonck, G. Labik, G. R. McKee, N. Schoenbeck, B. C. Stratton, I. Uzun-Kaymak, and G. Winz, "Overview of the beam emission spectroscopy diagnostic system on the National Spherical Torus Experiment," *Rev. Sci. Instrum.* **81**(10), 10D717 (2010); in 18th Topical Conference on High-Temperature Plasma Diagnostics, Wildwood, NJ, May 16–20, 2010.
- ⁴⁴D. R. Smith, R. J. Fonck, G. R. McKee, and D. S. Thompson, "Diagnostic performance of the beam emission spectroscopy system on the National Spherical Torus Experiment," *Rev. Sci. Instrum.* **83**(10), 10D502 (2012); in 19th Topical Conference on High-Temperature Plasma Diagnostics Monterey, CA, May 6–10, 2012.
- ⁴⁵J. A. Krommes, "Fundamental statistical descriptions of plasma turbulence in magnetic fields," *Phys. Rep.* **360**(1–4), 1–352 (2002).
- ⁴⁶V. Naulin, O. E. Garcia, A. H. Nielsen, and J. J. Rasmussen, "Statistical properties of transport in plasma turbulence," *Phys. Lett. A* **321**(5–6), 355–365 (2004).
- ⁴⁷J. A. Boedo, D. L. Rudakov, R. J. Colchin, R. A. Moyer, S. Krasheninnikov, D. G. Whyte, G. R. McKee, G. Porter, M. J. Schaffer, P. C. Stangeby, W. P. West, S. L. Allen, and A. W. Leonard, "Intermittent convection in the boundary of DIII-D," *J. Nucl. Mater.* **313**, 813–819 (2003); in 15th International Conference on Plasma-Surface Interactions in Controlled Fusion Devices (PSI-15), Gifu, Japan, May 26–31, 2002.
- ⁴⁸D. R. Smith, S. E. Parker, W. Wan, Y. Chen, A. Diallo, B. D. Dudson, R. J. Fonck, W. Gutfenfelder, G. R. McKee, S. M. Kaye, D. S. Thompson, R. E. Bell, B. P. LeBlanc, and M. Podesta, "Measurements and simulations of low-wavenumber pedestal turbulence in the National Spherical Torus Experiment," *Nucl. Fusion* **53**(11), 113029 (2013).
- ⁴⁹C. H. Knapp and G. C. Carter, "Generalized correlation method for estimation of time-delay," *IEEE Trans. Acoust., Speech, Signal Process.* **24**(4), 320–327 (1976).
- ⁵⁰S. J. Zweben, D. P. Stotler, R. E. Bell, W. M. Davis, S. M. Kaye, B. P. LeBlanc, R. J. Maqueda, E. T. Meier, T. Munsat, Y. Ren, S. A. Sabbagh, Y. Sechrest, D. R. Smith, and V. Soukhanovskii, "Effect of a deuterium gas puff on the edge plasma in NSTX," *Plasma Phys. Controlled Fusion* **56**(9), 095010 (2014).
- ⁵¹R. D. Durst, R. J. Fonck, G. Cosby, H. Evensen, and S. F. Paul, "Density fluctuation measurements via beam emission spectroscopy (invited)," *Rev. Sci. Instrum.* **63**(10), 4907–4912 (1992).
- ⁵²H. Evensen, D. Brouchous, D. Diebold, M. Doczy, R. J. Fonck, and D. Nolan, "Optical fluctuation measurements of turbulence using a diagnostic beam on Phaedrus-T," *Rev. Sci. Instrum.* **63**, 4928 (1992).
- ⁵³S. J. Zweben, J. McChesney, and R. W. Gould, "Optical imaging of edge turbulence in the Caltech tokamak," *Nucl. Fusion* **23**(6), 825 (1983).
- ⁵⁴J. A. Boedo, N. Crocker, L. Chousal, R. Hernandez, J. Chalfant, H. Kugel, P. Roney, J. Wertenbaker, and NSTX Team, "Fast scanning probe for the NSTX spherical tokamak," *Rev. Sci. Instrum.* **80**(12), 123506 (2009).
- ⁵⁵J. A. Boedo, J. R. Myra, S. Zweben, R. Maingi, R. J. Maqueda, V. A. Soukhanovskii, J. W. Ahn, J. Canik, N. Crocker, D. A. D'Ippolito, R. Bell, H. Kugel, B. LeBlanc, L. A. Roquemore, D. L. Rudakov, and NSTX Team, "Edge transport studies in the edge and scrape-off layer of the National Spherical Torus Experiment with langmuir probes," *Phys. Plasmas* **21**(4), 42309 (2014).
- ⁵⁶A. Kirk, N. Ben Ayed, G. Counsell, B. Dudson, T. Eich, A. Herrmann, B. Koch, R. Martin, A. Meakins, S. Saarelma, R. Scannell, S. Tallents, M. Walsh, H. R. Wilson, and MAST Team, "Filament structures at the plasma edge on MAST," *Plasma Phys. Controlled Fusion* **48**(12B), B433–B441 (2006); in 33rd European-Physical-Society Conference on Plasma Physics, Angelicum University, Rome, Italy, June 19–23, 2006 (Associazione EURATOM-ENEA Fusione; European Physical Society).
- ⁵⁷R. Scannell, A. Kirk, N. Ben Ayed, P. G. Carolan, G. Cunningham, J. McCone, S. L. Prunty, and M. J. Walsh, "Experimental investigation into ELM filament formation on MAST," *Plasma Phys. Controlled Fusion* **49**(9), 1431–1446 (2007).
- ⁵⁸T. Munsat, H. K. Park, I. G. J. Classen, C. W. Domier, A. J. H. Donne, J. Luhmann, N. C. E. Mazzucato, M. J. van de Pol, and TEXTOR Team, "Localization of the magnetic reconnection zone during sawtooth crashes in tokamak plasmas," *Nucl. Fusion* **47**(11), L31–L35 (2007).